ARTICLE

Check for updates

Rough capillary rise

Jack R. Panter [1,3,4], Andrew R. Konicek [2,4], Mark A. King[2], Arben Jusufi[2], Mohsen S. Yeganeh[2] &
Halim Kusumaatmaja [1 ✉]

Capillary rise within rough structures is a wetting phenomenon that is fundamental to survival
in biological organisms, deterioration of our built environment, and performance of numerous
innovations, from 3D microfluidics to carbon capture. Here, to accurately predict rough
capillary rise, we must couple two wetting phenomena: capillary rise and hemiwicking.
Experiments, simulations, and theory demonstrate how this coupling challenges our con-
ventional understanding and intuitions of wetting and roughness. Firstly, the critical contact
angle for hemiwicking becomes separation-dependent so that hemiwicking can vanish for
even highly wetting liquids. Secondly, the rise heights for perfectly wetting liquids can differ
between smooth and rough systems, even with the same 0° contact angle. Finally, the raised
liquid volumes are substantially increased in rough compared to smooth systems. To explain
and predict all rise heights and volumes with quantitative accuracy, we present the Dual-Rise
model that is valid for general roughness, liquids, and surface wettabilities.

[1] Department of Physics, Durham University, South Road, Durham DH1 3LE, UK. [2] Corporate Strategic Research, ExxonMobil Research and Engineering
Company, Annandale, NJ 08801, USA. [3] Present address: School of Engineering, University of East Anglia, Norwich, Norfolk NR4 7TJ, UK. [4] These authors
contributed equally: Jack R. Panter, Andrew R. Konicek. ✉email: halim.kusumaatmaja@durham.ac.uk

C apillary rise has long been considered a fundamental wetting phenomenon. Yet, the impact of surface roughness is poorly understood, even though all real surfaces have some degree of roughness. Occurrences of rough capillary rise are widespread and diverse, including water manipulation strategies in nature[1–6], weathering and deterioration in geology and our built environment[7–13], and fluid storage in fractured materials[14–16].

Rough capillary rise sees the coupling of two wetting phenomena: capillary rise between the walls, and hemiwicking within the surface roughness. Individually, capillary rise and hemiwicking are well understood. The long-established Jurin's law describes equilibrium capillary rise between smooth solid surfaces. This has been interpreted and refined by numerous luminaries such as Young and Laplace[17,18], Gibbs[19], and more recently de Gennes[20,21]. Regarding wetting of rough surfaces, the condition required for hemiwicking is also well established[22–25]. However, the maturity of these fields has regularly led to oversimplifications on the interplay between hemiwicking and capillary rise. This is evidenced throughout the literature on rough capillary rise dynamics, spanning an extraordinary range of fields such as porosity[26,27], earth science[28], biophysics[29], textiles[30,31] and engineering[7] to name but a few. Thus, there is a lack of fundamental understanding of rough capillary rise, leading to erroneous predictions of the rise heights.

Here, we provide a detailed analysis and explanation of equilibrium rough capillary rise. Principally, we take a rigorous energy minimisation approach to develop the Dual-Rise model, which is analytic and valid for general roughness. We demonstrate quantitative accuracy when compared to both experiments and simulations. In order to achieve the coupling between the two modes of liquid rise, we show that it is essential to capture the interaction between two length scales: the scale of the roughness, and the scale of the capillary wall separation.

In previous works, a key assumption has been that hemiwicking and capillary rise are independent phenomena[26,29–32]. However, this approximation breaks down at narrow surface separations. This has several consequences. Firstly, the critical angle for hemiwicking is often considered a thermodynamic criterion dependant on the property of the surface roughness and the liquid wettability[23–25]. In contrast, here we show that it also depends on the surface separation, and hemiwicking can be suppressed even for perfectly wetting liquids. Secondly, across this transition, the rise heights change abruptly, so that capillary rise depends strongly on the presence or absence of hemiwicking. This regime is particularly important to model accurately, as this is where the largest rise heights occur, and is typical in many of the rough rise occurrences and applications listed previously[1–16].

When predicting the capillary rise height, previous works typically assume that it is sufficient to treat the roughness in an effective manner by using the Cassie-Baxter[33] and Wenzel[34] models, used canonically across wetting physics. These approximations are attractive, as the roughness details are reduced to an effective contact angle which can then enter Jurin's Law, and so are widely used[9,28,29,32,35–37]. However, a key issue with both models is that they provide no information on their ranges of validity. We also find a further issue with the Wenzel model: this approximation strongly underestimates capillary rise when the predicted Wenzel angle is 0°, which occurs for even modest roughness and substrate wettability. Unfortunately, the Wenzel model is being widely used in this invalid regime, from fundamental rise predictions to the storage of liquid contaminants[22,28,29,36,37].

We also show that capturing the coupling between hemiwicking and capillary rise, and their two characteristic length scales, is vital for predicting the liquid volumes raised. Any variant of the Cassie-Baxter and Wenzel models is inaccurate, as they both ignore the hemiwicking contribution. Meanwhile, treating the surfaces as essentially smooth, used for example in[9,35], underestimates the total volume, which can be substantial on real surfaces.

Overall, this detailed understanding of equilibrium rough capillary rise will aid investigations in rise dynamics[29,32,38], and will be essential for the functionalisation of rough capillary rise currently being attempted. Innovations include controlling fluid localisation in 3D cellular fluidics[39,40], determining the extent and volume of liquid required for vascular cementitious repair[41], and designing novel carbon capture technologies based on liquid infused surfaces[42].

Results

Defining equilibrium. Here, we explore equilibrium rough capillary rise between parallel micropillared surfaces. A typical liquid rise morphology from simulations is shown in Fig. 1a, featuring both liquid rise between the plates, and hemiwicking within the surface texture.

In Fig. 1b, we distinguish two regions of liquid rise: the capillary region, which is separated into the capillary rise C and the meniscus M, and the hemiwicking region of height H. The total rise height T is the sum: $T = C + M + H$. Capillary rise is measured from the level of the reservoir ($z = 0$) at zero hydrostatic pressure, to the bottom of the meniscus. The meniscus height M is measured as the difference between the maximum and minimum heights of the liquid-gas interface between the two plates. The hemiwicking height H must be treated carefully. To illustrate the challenge, Fig. 1a shows how, at low contact angles, the hemiwicking region may exhibit an extended tail to large heights. The morphology of this tail is highly dependent on the specific roughness geometry[27,43]. However, as the energy minimisation will show in the proceeding section, a description of hemiwicking that is valid for general roughness can be obtained by using the centre of mass, H_{COM}, of the hemiwicking liquid, such that we define $H = 2H_{COM}$. This has the further advantage of always remaining a finite value. A direct benefit of this is that it resolves the issue of infinite rise height predictions in sharp grooves[44].

Perpendicular to the plates, there are two length scales we focus on throughout. The first, δ, is defined as the average cross-sectional depth of liquid in the hemiwicking region. Here, we approximate δ as a constant, and equal to the average roughness depth. The relationship between δ and the rough texture geometries used throughout is shown in Table 1. The second length scale is d, associated with the plate separation. d is the average distance separating two hemiwicked plates. The two length scales are related by the average perpendicular distance between the two rough surfaces, D, where $D = d + 2\delta$.

To describe rough textures generally, three parameters are defined: the roughness r, the area fraction ϕ, and the wetted fraction f. As an example, these parameters are expressed in Table 1 for the square and cylindrical pillars used throughout, where P is the pitch length, w_p is the pillar width for square pillars or pillar diameter for cylindrical pillars, and h_p is pillar height. r is defined as the ratio between the total surface area of the texture to the projected area. ϕ is defined in the hemiwicked region as the ratio between the projected area of dry solid to the projected total solid area. f is defined in the hemiwicked region as the ratio of the wetted solid surface area to the total solid surface area. On flat-topped, smooth-topped, non-overhanging structures, as used here, f can be simplified to $f = 1 - \phi/r$.

A complication in finding the equilibrium morphology via simulations and experiments is the presence of pinning. Pinning
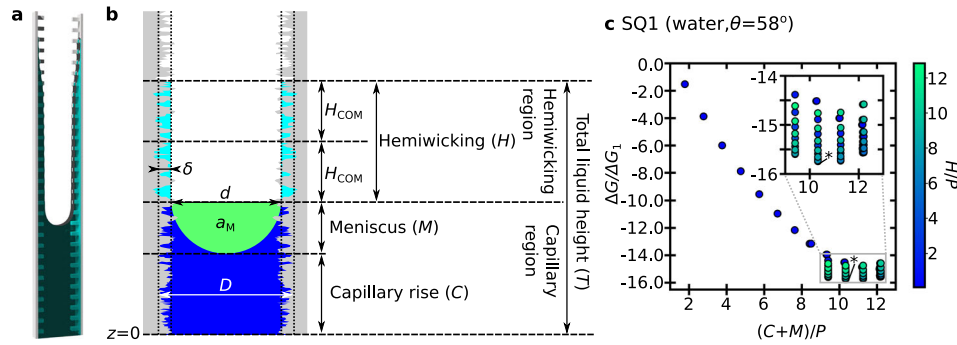
Fig. 1 Defining the equilibrium rise heights in rough capillary rise. a Archetypal simulated rise heights in a rough parallel plate setup, exhibiting capillary rise between the surfaces, a meniscus, and hemiwicking within the roughness. **b** Definition of the model geometric parameters. Shown are the rise heights of the: capillary rise C, meniscus M, hemiwicking H, centre of mass of hemiwicking liquid H_{COM}, and total liquid height T. Also shown are the length scales of the: average roughness depth δ, average distance between hemiwicking columns d, and average total plate separation D. The area above the meniscus in the capillary region is denoted a_M. Precise descriptions of all parameters are given in the text. **c** Plot of all metastable, pinned states observed for the simulated system SQ1 (detailed in methods, Table 4), featuring square posts with water as the rising liquid, $d/\delta = 5.43$, and contact angle $\theta = 58°$. The vertical scale shows the reduced energy variation (ΔG) when raising liquid from the reservoir to each unique pinned state, normalised against the energy of hemiwicking a single pitch length in the absence of gravity (ΔG_1). The normalised rise heights in the capillary region and hemiwicking region are indicated on the horizontal axis and colour scale respectively. The magnified inset highlights the density of metastable states around the global minimum energy state (the equilibrium state), indicated by '*'.

Table 1 The roughness parameters for a pillared texture, where the shape parameter $\alpha = 1$ for square pillars, and $\alpha = \pi/4$ for cylindrical pillars.

Parameter	Symbol	Expression
Average depth	δ	$h_p(1 - \alpha w_p^2/P^2)$
Roughness	r	$1 + 4\alpha w_p h_p/P^2$
Area fraction	ϕ	$\alpha w_p^2/P^2$
Wetted fraction	f	$1 - \alpha w_p^2/(P^2 + 4\alpha w_p h_p)$

leads to a large range of metastable states. To illustrate this, in Fig. 1c we examine all pinned states for a texture we study in detail throughout: SQ1, a square array of square pillars, with water as the rising liquid (see Methods, Table 4 for a full description of all systems and abbreviations). For a single value of the plate separation $\delta/d = 5.43$ and contact angle $\theta = 58°$, 73 metastable states are observed. Each state is distinguished via its rise height in the capillary region, $C + M$ (shown on the horizontal axis), and the hemiwicking height H (shown on the colour scale), normalised relative to the simulated pitch length P. The vertical scale shows the reduced energy change, which is the energy change of forming a given fluid configuration from an initially gas-filled system, ΔG, compared to the energy change of hemiwicking over a single pitch length from an initially gas-filled system ΔG_1. For this system, we see three important states. Firstly, the lowest-height metastable state occurs when the meniscus pins on the 2nd pillar up from the reservoir with no hemiwicking. This state would be observed if an initially dry texture was contacted with the reservoir, and the liquid allowed to rise quasi-statically without any perturbations. Secondly, at the opposite extreme in rise heights, the meniscus pins on the 12th pillar, with hemiwicking observed for another 12 pillars above this. This state would be observed if the system was initially submerged in water, and the liquid allowed to reach a static state by draining. Both of these states are strongly dependent on how the roughness geometry controls the shape of the pinned three-phase contact line[45]. However, our principal interest here is the third important state, the equilibrium state, which occurs at intermediate rise heights (denoted * in Fig. 1c and the magnification panel). In this state, capillary forces and weight

balance, so that pinning forces are minimal. It is not trivial to access the equilibrium state. In simulations, we must locate this state by finding the lowest energy configuration of all metastable states. In experiments, we do not have access to the energy directly, but instead perturb the system (tap the plates) to overcome the pinning barriers. This procedure is able to approximate the equilibrium state, with an estimated uncertainty of ± 1 pitch length.

Modelling equilibrium

The dual-rise model. We now develop the Dual-Rise model, to predict the equilibrium rough capillary rise. Taking an energy minimisation approach, we begin by constructing the energy change ΔG upon raising liquid from a reservoir to a configuration like that illustrated in Fig. 1a, and described in Fig. 1b,

$$\Delta G = \Delta A_{sg}\gamma_{sg} + \Delta A_{sl}\gamma_{sl} + \Delta A_{lg}\gamma_{lg} + \Delta E_g. \quad (1)$$

ΔA_{sg}, ΔA_{sl}, and ΔA_{lg} are the changes in the solid-gas, solid-liquid, and liquid-gas interfacial areas between the initial and final states respectively. ΔE_g is the change in gravitational potential energy associated with the difference in liquid centre of mass height between the two states. γ_{sg}, γ_{sl}, and γ_{lg} are the solid-gas, solid-liquid, and liquid-gas surface tensions respectively.

Each term in Eq. (1) is defined separately for the capillary and hemiwicked regions in Table 2. For this work, we consider long range surface interactions to be negligible compared to the interfacial energy and gravitational potential energy scales.

In order to produce an analytic and tractable model, we model the meniscus using the standard circular arc approximation. This is accurate for plate separations up to the order of the capillary length[46]. The curve has arclength l_M, and segment area a_M, shown as the green-shaded region in Fig. 1b. The centre of mass of this segment is located a distance z_M below $C + M$. We will show that the only meniscus property affecting the equilibrium rise heights is a_M. a_M, l_M, and z_M are illustrated in Supplementary Note 1 (Supplementary Fig. S1), with their standard analytic expressions given in Supplementary Eqs. (S1–S3) respectively.

After substituting the terms in Table 2 into Eq. (1), we minimise ΔG with respect to both C and H, under the constraint that $C, H, M, T > 0$. An interesting consequence of this procedure is that two classes of solutions emerge. These two solutions are distinguished by either $H = 0$, or $H > 0$. Thus, from our

Table 2 The free energy change contributions to ΔG arising from the capillary and hemiwicked regions.

	Capillary region	Hemiwicked region
ΔA_{sg}	$-2L(C+M)r$	$-2LHrf$
ΔA_{sl}	$2L(C+M)r$	$2LHrf$
ΔA_{lg}	$L(l_M - d)$	$2LH(1-\phi)$
ΔE_g	$\rho g L \frac{D}{2}(C+M)^2$	$2\rho g \delta L H \left(C+M+\frac{H}{2}\right)$
	$-\rho g L a_M (C+M-z_M)$	

minimisation scheme, the conditions for observing hemiwicking above the meniscus are defined. This important feature of the Dual-Rise model contrasts with the Cassie-Baxter and Wenzel effective-angle models, in which the hemiwicking state has to be known a priori.

Overall, the defining equations of the Dual-Rise model are:

$$
C = \begin{cases} \frac{2\lambda_c^2}{D} r \cos\theta - M + \frac{a_M}{D} & \text{if } H = 0, \\ \frac{2\lambda_c^2}{d} \cos\theta^* - M + \frac{a_M}{d} & \text{otherwise,} \end{cases} \quad (2)
$$

$$
H = \frac{\lambda_c^2}{\delta}\left(r\cos\theta - \cos\theta^* - \frac{2\delta}{d}\cos\theta^*\right) - \frac{a_M}{d}, \quad (3)
$$

and

$$
T = \begin{cases} \frac{2\lambda_c^2}{D} r \cos\theta + \frac{a_M}{D} & \text{if } H = 0, \\ \frac{\lambda_c^2}{\delta}(r\cos\theta - \cos\theta^*) & \text{otherwise,} \end{cases} \quad (4)
$$

where, by the circular arc approximation,

$$
M = \frac{d(1 - \sin\theta_M)}{2\cos\theta_M}. \quad (5)
$$

λ_c is the capillary length, $\lambda_c = \sqrt{\gamma_{lg}/(\rho g)}$ where ρ is the liquid density and g is the acceleration due to gravity. θ is the contact angle of liquid on a smooth solid substrate, and θ^* is the Cassie-Baxter effective contact angle for liquid on a liquid-filled rough substrate[33],

$$
\cos\theta^* = r(1-f)\cos\theta + 1 - \phi, \quad (6)
$$

For the meniscus contact angle, θ_M, this must be defined for when hemiwicking is present and absent. A simple approximation is to use

$$
\theta_M = \begin{cases} \theta^* & \text{if } \theta \le \theta_c, \\ \theta_W & \text{if } \theta \ge \theta_c, \end{cases} \quad (7)
$$

where θ_c[22,23] is the critical angle for hemiwicking,

$$
\cos\theta_c = (1-\phi)/(fr), \quad (8)
$$

and θ_W is the Wenzel effective contact angle for wetting on a rough surface[34],

$$
\cos\theta_W = r\cos\theta. \quad (9)
$$

We note that an improved approximation for θ_M could be achieved by replacing θ_c in the two case conditions in Eq. (7) with the contact angle at which $H = 0$ in Eq. (3). However, this does not produce a closed set of equations for the rise heights, and we will show throughout that M in Eq. (7) is already sufficiently accurate. Further justification of our treatment of θ_M is shown in Supplementary Fig. S2.

It will prove most instructive to discuss the physical significance of each of these equations with reference to simulation and experimental data in the following section.

Dual-Rise dependence on separation. We begin by examining in detail the different modes of liquid rise in system SQ1, with water as the rising liquid and $\theta = 58°$, as the plate separation d is varied. In Fig. 2a, three characteristic regimes of liquid rise are identified. The quantitative variation of the rise heights with plate separation is shown in Fig. 2b.

At the largest plate separations, labelled regime 1 in Fig. 2a, b, the two rough surfaces are essentially non-interacting. This means that capillary rise is negligible, and the hemiwicking and meniscus heights are equivalent to those observed on a single, rough plate. Rise data for the single plate is shown at the extreme right of Fig. 2b. For the meniscus, the small rise height M measured in experiments (2.1 ± 0.7) mm, and simulations (2.8 ± 0.7) mm, is consistent with the analytical prediction of 2.6 mm from $M = \lambda_c\sqrt{2(1 - \sin\theta_M)}$[47]. The ± 0.7 mm uncertainty in both simulations and experiments is the ± 1 pitch length uncertainty associated with pinning to the discrete posts in system SQ1. Adding the hemiwicking height to the meniscus yields the total rise height T, determined as (11.5 ± 0.7) mm and (11.6 ± 0.7) mm from experiment and simulations respectively. These are in agreement with the Dual-Rise prediction in Eq. (4) for $H > 0$, $T = 12.1$ mm. Examining Eq. (4) further, we observe that the energy minimisation has reproduced the heuristic balance of forces per unit length of the contact line between capillarity acting upwards, $\gamma_{lg}(rf\cos\theta - 1 + \phi)$, and weight acting downwards, $\rho g \delta T$, used previously to estimate T on a single plate[22]. However, the derivation of the Dual-rise model reveals that this estimate of T is not an estimate of the maximum height obtained, but is actually associated with the centre of mass of the hemiwicked liquid, as we discussed in Section 'Defining Equilibrium'. Although this distinction is minimal for system SQ1 at modest wettabilities, it becomes substantial for highly wettable surfaces.

As the plates are brought closer together, the capillary rise height grows monotonically, while hemiwicking decreases. A typical configuration is shown in Fig. 2a, labelled regime 2. In Fig. 2b, we also see that the total rise height remains independent of the plate separation throughout regime 2. Indeed, there is no difference in total rise height between a single rough plate, and a rough capillary when hemiwicking is present. In the heuristic force balance above, the dominant approximation was that the hemiwicking height was independent of the capillary rise. In this regime, both Dual Rise and the data in Fig. 2b show this assumption to be accurate. Likewise, if we examine the Dual-Rise prediction for C when $H > 0$ in Eq. (2), aside from a meniscus contribution, C could be derived by considering liquid rising over two pre-hemiwicked surfaces of separation d, in which the contact angle is given by the Cassie-Baxter effective contact angle for the composite liquid-filled surfaces, θ^*. Thus in regime 2, we also verify that C can be predicted independently from H. Overall, this explains the range of previous experimental observations of the mutual independence of capillary rise and hemiwicking, across such fields as textiles[30,31], bioinspired design[29] and porous media[26,32].

However, at close plate separations, when the separation and roughness length scales become comparable, a threshold is reached where capillary rise overtakes the top of the hemiwicked column. For system SQ1, Fig. 2b shows this to occur at $\log_{10}(d/\delta) = 0.5$, equivalent to $d = 0.75$ mm. Here, the independence of capillary rise and hemiwicking breaks down, as suddenly the total rise height changes from being constant, to now increasing as the plate separation decreases. The example of regime-3 shown in Fig. 2a illustrates the absence of hemiwicking. To the best of our knowledge, observations of this regime have not been made previously, despite the largest rise heights occurring here. Regime 3
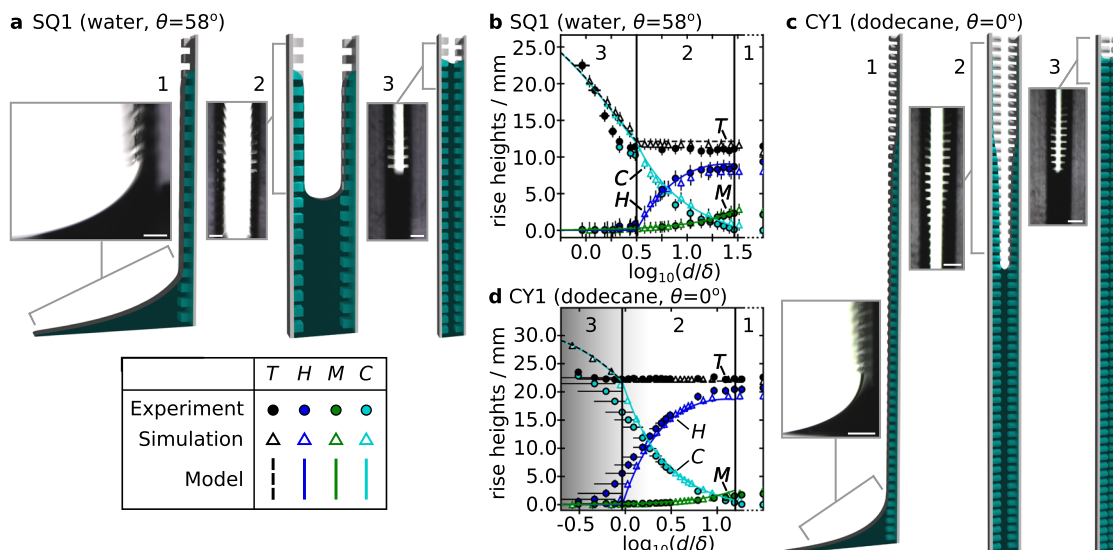
Fig. 2 The variation of the rough capillary rise heights with plate separation, compared between experiments, simulation, and theory. a Examples of the three regimes of rough capillary rise on system SQ1, a square-pillared system with water as the rising liquid (capillary length $\lambda_c = 2.7$ mm) and contact angle $\theta = 58°$. Full images are simulation results, with insets showing magnifications of equivalent experimental systems on the region of interest. Scale bars $= 1$ mm. **b** Plot of the variation in the rise heights with plate separation d (normalised relative to the roughness depth δ) for system SQ1, where $\delta = 326\,\mu$m, separated into the three regimes. The capillary rise C, meniscus M, hemiwicking H, and total liquid height T, are labelled. Experimental data are shown as filled circles, with horizontal error bars indicating measured separation uncertainty, $\pm 50\,\mu$m, and vertical error bars the ± 1 post pinning uncertainty, $\pm 709\,\mu$m. Simulation data are shown as empty triangles with vertical error bars indicating the ± 1 post pinning uncertainty. Data at the extreme right indicate the rise heights on a single plate, equivalent to infinite plate separation. The Dual-Rise predictions are shown as lines. **c** Example images of the three regimes of rough capillary rise on system CY1, a cylindrically-pillared system with dodecane as the rising liquid (capillary length $\lambda_c = 1.8$ mm), and contact angle $\theta = 0°$. Scale bars $= 1$ mm. **d** Plot of the variation in the rise heights with plate separation for system CY1, where $\delta = 325\,\mu$m. The shaded region indicates where the separation uncertainty (horizontal error bars) in the experimental data becomes large. The vertical ± 1 post pinning uncertainty is $\pm 458\,\mu$m.

therefore has particular relevance to the range of applications mentioned previously that aim to exploit or control rough capillary rise[1–16].

Often in the rise dynamics literature, the measure for describing whether hemiwicking will be observed is the critical angle θ_c, defined in Eq. (8). If $\theta < \theta_c$, hemiwicking is observed. Eq. (8) can be derived by considering the energy change when raising liquid above the surface of a reservoir at zero hydrostatic pressure, and in the absence of gravity. However, when there is hemiwicking from the top of a capillary-risen column, the change in gravitational potential energy must also be taken into account. Now, the criterion for hemiwicking becomes more complicated, and in general must be solved numerically by setting $H = 0$ in Eq. (3). However, if the meniscus is small compared to capillary rise, this results in the condition for hemiwicking on rough plates,

$$\cos\theta_{H=0} = \frac{\cos\theta_c}{1 - \frac{2\delta}{fD}}. \qquad (10)$$

We may also interpret this equation by asking what is the hydrostatic pressure required to be applied to overcome the capillary pressure favouring hemiwicking[48]. The capillary pressure favouring hemiwicking is $\gamma_{lg}(rf\cos\theta - 1 + \phi)/\delta$, and the hydrostatic pressure at the top of the capillary-risen column is $-\rho g C$. Equating these two pressures and substituting either case for C from Eq. (2), produces Eq. (10) in the limit that the meniscus is small. A key feature of Eq. (10) is that the denominator can always be made arbitrarily small, so that hemiwicking is always lost by bringing the plates close together. This represents an important design consideration for systems with closely-spaced plates, such as solar desalinators[49], water purification devices[50], and liquid-infused carbon capture[42]. The

challenge in these applications is to maximise the liquid-gas surface area through hemiwicking, while maintaining a high plate packing density (close wall separations).

We now test the claim that the observations presented so far and the Dual-Rise model are valid generally. In Fig. 2c, d, we replicate the analysis for system SQ1, but this time for system CY1, featuring cylindrically-pillared surfaces, with dodecane as the rising liquid and a contact angle $\theta = 0°$. Further details of this system are given in Methods, Table 4. An extended validation of the Dual-Rise model is further shown in Supplementary Note 2 (see Supplementary Fig. S3), where we vary the system scale, each pillar dimension, and also include a vertical groove geometry. These are summarised in Supplementary Table 1.

For system CY1, we observe the same three regimes of liquid rise, shown in Fig. 2c. For this system, when hemiwicking is present (regimes 1 and 2), an elongated tail is observed up to large rise heights. The Dual-Rise model for hemiwicking however remains accurate, as shown in Fig. 2d. In this region, CY1 also shows a constant total rise height, $T = 22.0$ mm. On decreasing the plate separation, we observe the hemiwicking transition to regime 3, at a separation $\log_{10}(d/\delta) = -0.046$, equivalent to $d = 0.30$ mm. There is an interesting interplay between the two length scales. In the roughness, gravity causes the hemiwicking height to be finite, which is in direct contrast to the complete spreading of perfectly wetting liquid on a single, horizontal plate. Between the plates, this finite hemiwicking height is then able to be exceeded by capillary rise at sufficiently small plate separations. In regime 3, the Dual-Rise model is also shown to accurately capture the simulation observations. Note that for experiments, the small plate separation in this region means that the separation uncertainty, caused by small deviations in the plate alignment and measurement precision, becomes relatively large, so that simulations become the more reliable comparison.
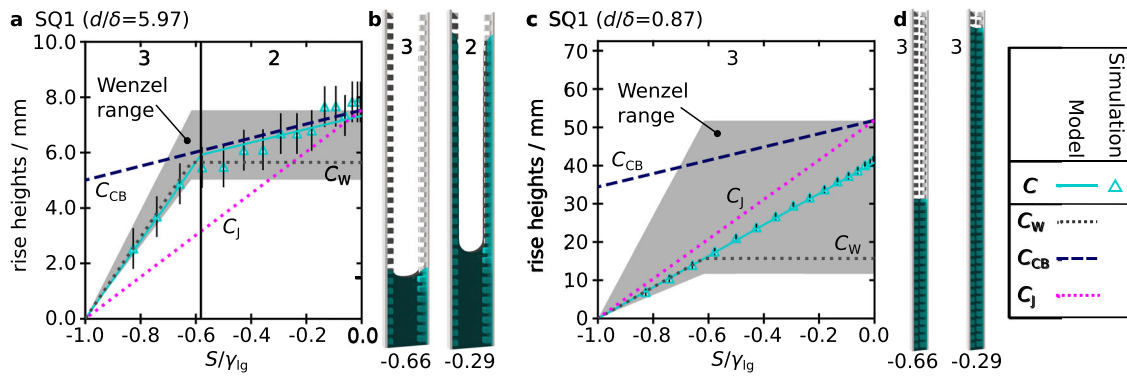
Fig. 3 Capillary rise against gravity between two rough plates of variable wetting parameter, S. a Comparison of the capillary rise heights between the: Dual-Rise Model, C, Jurin's Law, C_J, and the apparent angle approximations, C_W (Wenzel approximation) and C_{CB} (Cassie-Baxter approximation), for the simulated square-pillared system SQ1 at a moderate value of the plate separation to roughness depth ratio ($d/\delta = 5.97$). The rising liquid is water ($\lambda_c = 2.7$ mm), and we vary the substrate wettability S (normalised with respect to the liquid-gas interfacial tension γ_{lg}). The shaded region indicates the range of possible Wenzel capillary rise predictions when varying the plate separation, x, in Eq. (13). Error bars in the simulated data indicate the ± 1 post uncertainty. **b** Example equilibria at $d/\delta = 5.97$ in region 3, $S/\gamma_{lg} = -0.66$ ($\theta = 70°$), and region 2, $S/\gamma_{lg} = -0.29$ ($\theta = 45°$). **c** Model comparison with the simulated system SQ1 at narrow plate separation ($d/\delta = 0.87$). **d** Example equilibria at $d/\delta = 0.87$ in region 3 at $S/\gamma_{lg} = -0.66$ ($\theta = 70°$), and $S/\gamma_{lg} = -0.29$ ($\theta = 45°$).

From partially wetting to perfectly wetting systems. In the previous section, we explored how changing the plate separation, roughness parameters, and liquid properties influenced the rise heights. Now, we examine the effect of changing the surface wettability, described via the spreading parameter S ($S = \gamma_{lg}(\cos\theta - 1)$). This is summarised in Fig. 3 as we study the capillary rise C for system SQ1, where water is used as the rising liquid ($\lambda_c = 2.7$ mm).

In Fig. 3a the plate separation is fixed at a moderate value, $d/\delta = 5.97$ (equivalently $d = 1.99$ mm). This system exhibits a hemiwicking transition at $S/\gamma_{lg} = -0.58$ (equivalent to $\theta = 65°$). At large, negative S (large contact angles) $H = 0$, with an example of a system in regime-3 shown in Fig. 3b at $S/\gamma_{lg} = -0.66$ ($\theta = 70°$). In this region, the meniscus is small, and capillary rise C increases linearly with S. The Dual-Rise model in Eq. (2) matches this observation: in the limit of small menisci, $C \propto \cos\theta \propto S$. Increasing S across the hemiwicking transition, we see a sudden reduction in the gradient of C, but the linear trend is maintained. An example system in this regime is shown in Fig. 3b at $S/\gamma_{lg} = -0.29$ ($\theta = 45°$).

As was shown by Eq. (10), hemiwicking can always be entirely suppressed by choosing a small enough plate separation. An example of this type of system is shown in Fig. 3c by choosing $d/\delta = 0.87$ ($d = 0.29$ mm). No hemiwicking is observed over the entire range of wettabilities, with example liquid configurations shown in Fig. 3d at $S/\gamma_{lg} = -0.66$ and -0.29.

An important aim of this work is to compare the capillary rise prediction C from the Dual-Rise model with commonly used effective contact angle adaptations to Jurin's law. We begin with Jurin's law for smooth surfaces, C_J,

$$C_J = \frac{2\lambda_c^2 \cos\theta}{d}. \qquad (11)$$

In Fig. 3a (for $d/\delta = 5.97$), we see that C_J is a poor approximation for C, except in two instances. The first (trivial) case is at $S/\gamma_{lg} = -1.0$ ($\theta = 90°$), in which C and C_J are identically 0. The second however occurs at $S/\gamma_{lg} = 0$ ($\theta = 0°$). This is because here, hemiwicking is present, so that the capillary rise is perfectly shielded from the surface roughness. In contrast, the system in Fig. 3c (for $d/\delta = 0.87$) never exhibits hemiwicking. At $S/\gamma_{lg} = 0$, the rising liquid is not shielded from the surface roughness, so Jurin's law is inaccurate at estimating C.

To adapt Jurin's law for rough surfaces, a common approximation is to substitute the contact angle θ in Eq. (11) with an apparent contact angle, derived either from a Cassie-Baxter or Wenzel treatment of the surface. When hemiwicking is present, the Cassie-Baxter model would be conventionally employed. Examples demonstrating this are refs. [29,32], with the limitation that they further approximate the Cassie-Baxter angle as 0°, which is not generally the case. The Cassie-Baxter height is given by

$$C_{CB} = \frac{2\lambda_c^2 \cos\theta^*}{d}, \qquad (12)$$

where the θ^* is the Cassie-Baxter angle for liquid rising over a composite liquid-filled solid texture, defined in Eq. (6). The Dual-Rise model in Eq. (2) reduces to Eq. (12) under the conditions that hemiwicking is present and the meniscus is vanishingly small. These conditions are fulfilled in regime 2 in Fig. 3a, so that C_{CB} accurately approximates C. The common justification of using the Cassie-Baxter model, that capillary rise occurs between two pre-hemiwicked plates, is therefore supported in regime 2. However, when hemiwicking is absent, this approximation breaks down causing C_{CB} to overestimate C, as shown in regime 3 of Fig. 3a, c. A key issue with this approximation is that the region of validity cannot be predicted by the Cassie-Baxter model, so that the hemiwicking state must be known a priori.

In the absence of hemiwicking, the Wenzel approximation models the effect of roughness with the Wenzel apparent contact angle θ_W, defined in Eq. (9). The Wenzel approximation for rough capillary rise at a plate separation x is

$$C_W(x) = \frac{2\lambda_c^2 \cos\theta_W}{x}. \qquad (13)$$

However, the Wenzel approximation does not reveal the suitable choice of the effective separation x, as the physical details of the roughness are ignored. The choice of x substantially influences the predicted rise height. The minimum reasonable x is when the plate separation is measured between the tops of the surface texture ($x = d$), whereas the maximum x would be the distance between the texture bottoms ($x = d + 2h_p$). This range leads to the large, grey, shaded regions in Fig. 3a, c. However, the Dual-Rise model suggests that the correct definition of the plate separation in the absence of hemiwicking should be the average total separation D. We label this special case $C_W(D)$ simply as C_W. In regime 3 of Fig. 3a, C_W
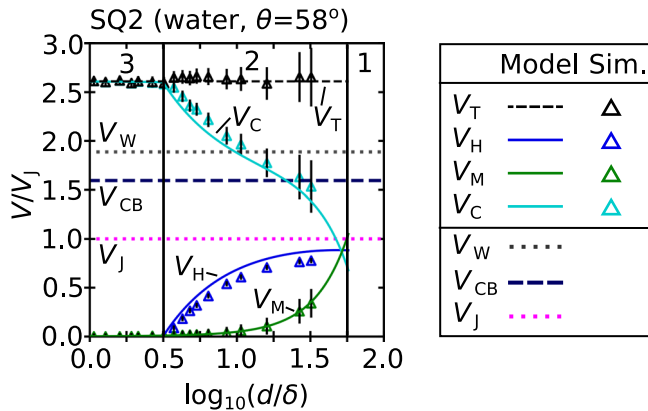
Fig. 4 The liquid volume raised against gravity upon variation of the plate separation. Predicted volumes from the Dual-Rise model are compared for the simulated, square-pillared system SQ2 with water as the rising liquid (capillary length $\lambda_c = 2.7$ mm) and $\theta = 58°$. The total volume V_T is shown, which is decomposed into the individual contributions from: capillary rise V_C, hemiwicking V_H, and the meniscus V_M. The ±1 post error bars are shown, and the plate separation d is shown relative to the roughness depth δ. Also shown are the capillary volumes calculated using: Jurin's Law V_J, the Wenzel approximation V_W, and the Cassie-Baxter approximation V_{CB}. The three regimes of equilibrium rise are demarked and labelled 1–3.

accurately estimates C, and as hemiwicking is present in regime 2, the Wenzel model becomes invalid.

In Fig. 3c, since hemiwicking is never present, we would naively expect the Wenzel model to be accurate across the range of spreading parameters. However, we find this is not true. C_W is accurate at large, negative S, but incorrectly plateaus for $S/\gamma_{lg} > -0.62$ ($\theta < 67°$). C_W now substantially underestimates C. This discrepancy grows, until at $S/\gamma_{lg} = 0$, C is a factor of r greater than C_W. This error occurs because the Wenzel angle in Eq. (9) is limited to 0° for all $r\cos\theta \geq 1$. In the Dual-Rise model, C in Eq. (2) shows that no such limit occurs in the $r\cos\theta$ term, arising from the capillary force of the rough surface. Importantly, this reveals that a wide range of published works, ranging from fundamental studies of porous rise to earth science, are using the Wenzel model in conditions where it is invalid (namely $r\cos\theta > 1$), see for example refs. [22,28,29,36,37].

We further reflect that there is a contrast between capillary rise on rough and smooth surfaces. According to de Gennes[20], in a smooth capillary the rise height plateaus for all spreading parameters where $\theta = 0°$ (i.e. $S \geq 0$). However, the rough equivalent is not true: the rough capillary rise height does not plateau for all spreading parameters where the Wenzel angle $\theta_W = 0°$. This contrast arises because on a smooth surface, the contact angle saturation is caused by a capillary force saturation due to a thin film shielding the capillary-rise liquid from the surface wettability. However, on a rough surface in the absence of hemiwicking, the Wenzel angle saturation does not imply a saturation of the capillary force, which instead continues to increase as $r\cos\theta$.

The volume of liquid raised. When computing the volume of liquid raised in a rough capillary, explicitly accounting for liquid in the roughness is of paramount importance. In Fig. 4, we plot the total volume raised V_T, as the sum of capillary, meniscus, and hemiwicking contributions, V_C, V_M, and V_H respectively, for the simulated system SQ2 with water as the rising liquid (capillary length $\lambda_c = 2.7$ mm) at $\theta = 58°$. Experiments and simulations for systems of different geometry are shown in Supplementary Note 2 (see Supplementary Fig. S4).

Table 3 Summary of model accuracies for hemiwicking H, capillary rise C, total liquid height T, and total volume V_T.

	$H=0$				$H>0$			
	H	C	T	V_T	H	C	T	V_T
Dual-Rise	✓	✓	✓	✓	✓	✓	✓	✓
Jurin	×	×	<	×			×	<	<
Wenzel ($\theta_W > 0°$)	✓	✓	✓		>	<	✓
Wenzel ($\theta_W = 0°$)	<	<	<		>	<	✓
Cassie-Baxter	>	>	×		✓	<	×

For each model, the symbols indicate whether a property is: predicted accurately (✓), always overestimated (>), always underestimated (<), inaccurate (×), or not predicted by the model (blank cell). θW is the Wenzel angle.

The principal striking feature of Fig. 4 is that V_T is constant across the range of plate separations, even though the distributions within the capillary and hemiwicking regions change, including across the hemiwicking transition. This separation independence is validated by the Dual-Rise model, where $V_T/L = DC + (DM - a_M) + 2\delta H$. L is an arbitrary portion of the infinite parallel plates. Upon rearrangement, the separation independence is made clear:

$$\frac{V_T}{L} = 2\lambda_c^2 r\cos\theta. \quad (14)$$

A second surprising feature is that the raised volume is substantially larger than would be predicted via all previous models. A smooth approximation $V_J = 2L\lambda_c^2\cos\theta$, underestimates the raised volume by a factor of the roughness parameter r, which can be large for real surfaces. Technologies relying on a smooth approximation are therefore considerably underestimating the total raised volume[9,35]. However, even the Wenzel model, $V_W = 2L\lambda_c^2\cos\theta_W$, underestimates the raised volume in Fig. 4 by almost 40%, as $r\cos\theta > 1$. The Cassie-Baxter model, $V_{CB} = 2L\lambda_c^2\cos\theta^*$, is always unreliable, as the hemiwicked volume is not accounted for.

Indeed, the interaction between the hemiwicked volume and capillary volume is key to explaining the separation independence of V_T. The capillary force that raises the liquid depends only on the surface properties, not the plate separation. At equilibrium, this must therefore always be balanced by the same weight of liquid. The weight of the hemiwicked column and meniscus displace an equal weight of liquid from the capillary region. As we treat the liquid as incompressible throughout, this means the raised volume is always independent of plate separation.

We consider again Fig. 2b, d, where the plate separation is increased across the hemiwicking transition, from regime 3 to regime 2. We can now use the separation independence of V_T to explain the sudden change in slope of C. On increasing the plate separation, the slope becomes steeper as hemiwicking suddenly emerges. In order to preserve the total volume, liquid must be drained from the capillary region into the hemiwicking region. Thus, C decreases faster upon the appearance of hemiwicking, than before hemiwicking emerges.

Conclusions
In this work, all contributions to equilibrium rough capillary rise are explained and predicted with quantitative accuracy by the Dual-Rise model, a model derived from a rigorous energy minimisation that is valid for surfaces of general roughness. A summary comparing our model accuracy is shown in Table 3, with Jurin's Law for smooth surfaces, and the Cassie-Baxter and Wenzel approximations for rough surfaces. Table 3 highlights

many ways in which these approximations inaccurately predict liquid heights and volumes, and indicates the limited cases where those rough surface approximations are accurate.

From this study, a number of interesting questions emerge that depend on the specific roughness geometry. For instance, how does the complex interplay between capillarity, hydrostatic pressure and the roughness geometry determine the curved morphology of the hemiwicking liquid-gas interface, and in particular how does this curvature affect the maximum liquid height? The roughness geometry is also crucial for pinning, leading to a range of metastable rise configurations. Can the pinning forces be predicted in both the hemiwicking and capillary regions?

We anticipate that the Dual-Rise model will play an important role in a broad range of applications in which liquid rise is to be predicted or controlled. In particular, we highlight its relevance in novel sustainability technologies, such as catalytic or carbon capture systems using Liquid Infused Surfaces[42], and in understanding and improving the lifespan of concrete structures[41].

Methods

System parameters. All experimental and simulated systems are listed in Table 4, indicating the roughness parameters, capillary length relative to the pitch P, and the pitch length P. Where both simulated and experimental equivalents of the same system are used, we match the simulated parameters as closely as possible to the experimental parameters. A small discrepancy is introduced, as an exact translation of the experimental system is not possible due to the simulation being composed of discrete cubic lattice points. This small discrepancy is within the reported error bars. For system CY1, to simulate very close surface separations ($\log_{10}(d/\delta) \leq 0.12$) required increasing the system size by 4 times in each direction, indicated as 'Sim. $4 \times$' in Table 4.

Two different rising liquids are used: water (distilled to a resistance of 18 MΩ, with surface tension $\gamma = 72$ mN m^{-1}, density $\rho = 1000$ kg m^{-3}, and capillary length $\lambda_c = 2.7$ mm); or dodecane (Sigma Aldrich, 99% purity, $\gamma = 24$ mN m^{-1}, $\rho = 745.2$ kg m^{-3}, $\lambda_c = 1.8$ mm).

In experiments, the textured plates were additively manufactured using Accura ClearVue resin (polycarbonate-like material). Plasma-treating the printed plates for 2 min on a high RF setting (Harrick Plasma, PDC-32G) energises the surface and alters the wettability. Plasma-treated smooth polycarbonate has a measured contact angle of 0° with dodecane, and 36° with water. With water, the additively manufactured roughness altered the contact angle on different faces of the posts of SQ1. The Dual-Rise model fits experimental rise heights at $\theta = 58°$, which was the contact angle also input into simulations. The quantitative agreement between theory, simulations, and experiments, justifies this choice of θ.

Liquid rise experiments. The textured plates were additively manufactured in a high resolution stereolithography process (3D Systems On Demand). Printed parts had the supports removed, were washed, but had no post-printing thermal cure and as such were left with a natural finish. The plates were 5 cm × 5 cm with a 3 mm thick backbone on which were either printed square cross-section posts 400 μm in diameter with a spacing of 300 μm (or a post-center-to-post-center pitch of 700 μm) or cylindrical cross-section posts 300 μm in diameter with a spacing of 150 μm (or a post-center-to-post-center pitch of 450 μm). Topographic measurements were carried out using a Leica DCM8 confocal profilometer using the 5 × objective, which was sufficient to resolve the post geometries. The target print

Table 4 Surface geometry and liquid parameters used in experiments and simulations.

System	r	f	ϕ	δ/P	λ_c/P	P
SQ1	2.61	0.87	0.34	0.46	3.82	Exp.: 708.5 μm Sim.: 40 L.U.
SQ2	2.61	0.87	0.33	0.47	7.67	Sim.: 40 L.U.
CY1	3.17	0.90	0.33	0.71	3.96	Exp.: 458 μm Sim.: 32 L.U. Sim. 4 ×: 128 L.U.

The system label 'SQ' refer to a square array of square pillars, 'CY' refers to a square array of cylindrical pillars. The listed parameters are: the roughness r, wetted area fraction f, area fraction ϕ, average roughness depth δ, capillary length of the liquid λ_c, and pitch length P. All parameters are defined precisely in the text. In the pitch length P column, experimental pitch lengths are indicated 'Exp.', and simulations 'Sim.', where 'L.U.' refers to lattice units (1 L.U. is 1 grid spacing).

height was 500 μm and measured values in randomly sampled regions were within 10% of that value. Target pillar pitch values were typically within 2% of the design size. The greatest variation came from post widths where all posts, regardless of shape or size, had a tapered as-manufactured shape, being narrower at the top and wider at the bottom. Mean diameters, taken as an average of the measured top diameter and bottom diameter, were within 10% of design specification, but varied up to 20% from the mean towards the narrower or wider end.

The experimental apparatus holds two of the textured plates, each of the same texture geometry, parallel to one another at a controlled and measured separation. This is accomplished using two micrometers attached orthogonally under one plate mount. One can be used to exactly align the columns of pillars (to better match the simulation) and the other controls the spacing between plates. A reservoir with the liquid can be raised and brought into contact with the lower portion of the plates. Liquid height measurements and profiles are measured using a camera (FLIR CCD camera equipped with an Infinity Photo-Optical Infiniprobe ms lens) viewing down the space between the plates. A bright light is placed on the far side of the plates such that the illumination provides a sharp contrast to the image. Areas occluded by the texture or by liquid appear dark, and all empty space is light. By moving the camera up and down (on an elevator attached to a digital micrometer), or side to side, the heights of the capillary and hemiwicked areas can be measured relative to the height of the liquid reservoir.

The initial plate separation is set to 10 mm. At this distance the separation is much larger than the capillary length for either liquid (water or dodecane), meaning that there is negligible communication between the meniscus that forms on either plate. The camera is centred on the flat liquid region and the elevator micrometer is zeroed. Then images are captured of the meniscus region as well as the maximum hemiwicked regions on either plate. The experiment proceeds as the plates are successively brought closer together, capturing images of the meniscus and hemiwicked regions and recording the camera height positions at one plate spacing before bringing them closer together. The main experimental challenge is the pinning that occurs as the bulk meniscus rises when the plates are brought closer together. Because of the periodic nature of the texture, there is a strong tendency for the meniscus contact line to pin on the top of one row of pillars before snapping up to wet the next row. In order to perturb the system into a lower energy configuration, we tap both the mount holding one of the plates (to perturb the plate spacing) as well as the stage holding the liquid reservoir (to perturb the liquid level). This tapping, especially at close plate separation, can cause the meniscus to jump up one or more rows, and the recorded images are taken at the locations where any further tapping will not move the liquid-gas interface. Further details of how the rise heights were measured from recorded images are shown in Supplementary Note 3.

Phase field simulations. The simulations we perform minimise the free energy of a diffuse-interface model with fluid-fluid interactions, in a gravitational field. We choose the diffuse interface model firstly to avoid making assumptions about the liquid-gas interface morphology or topology, requiring no special treatment for interfaces splitting or merging[51], and secondly to enable facile interactions between fluids and complex surface topographies[52,53].

For the cylinder-pillared systems, we use a ternary phase field model based on refs. [54,55]. Here, we use three order parameters, $C_1(\mathbf{r})$, $C_2(\mathbf{r})$, and $C_3(\mathbf{r})$, which define the local composition of the solid, liquid, and gas respectively. Note that the total composition is normalised, so that $C_1(\mathbf{r}) + C_2(\mathbf{r}) + C_3(\mathbf{r}) = 1$. A value $C_i(\mathbf{r}) = 0$ indicates no quantity of component i is present, whereas $C_i(\mathbf{r}) = 1$ indicates pure component i. We treat the solid in the posts in this diffuse manner, based on a previous model[56], to enable the creation of smooth, curved solids, while maintaining the cubic discretisation of the simulation domain. The solid surface at the base of the pillars is treated via a boundary condition, not a diffuse interface treatment.

The total free energy is expressed

$$\Psi[\{C_i(\mathbf{r})\}] = \int_v \left(\psi_b + \psi_\nabla + \psi_\Lambda + \psi_g \right) dv + \int_s \psi_s ds. \tag{15}$$

where the integrals are over the volume v and solid surface s. ψ_b is the bulk energy,

$$\psi_b = \frac{6}{\epsilon} \sum_{i=1}^3 \left(-S_i C_i^2 (1 - C_i)^2 \right), \tag{16}$$

and ψ_∇ is the gradient energy density,

$$\psi_\nabla = \frac{3}{8} \epsilon \left[\sum_{i=1}^3 -S_i |\nabla C_i|^2 \right]. \tag{17}$$

ϵ is the interface width. S_i defines the spreading parameter of phase i over the interface between phases j and k,

$$S_i = \gamma_{jk} - (\gamma_{ij} + \gamma_{jk}). \tag{18}$$

To enable complete spreading while maintaining simulation stability, the stabilisation term ψ_Λ is used[54],

$$\psi_\Lambda = \Lambda C_1^2 C_2^2 C_3^2, \tag{19}$$

where the parameter Λ is set to 50. The gravitational potential energy density, ψ_g is

defined

$$\psi_g = f_g C_2 z. \tag{20}$$

f_g is the gravitational force density, and acts as the conversion factor between the dimensional units in experiment and the nondimensional units in simulation: $f_g = \rho g \gamma' P^2/(\gamma P'^2)$, where ρ is the liquid density, g is the acceleration due to gravity, P and P' are the pitch lengths of the periodic surface roughness in real and lattice units respectively, γ and γ' are the liquid-gas interfacial tensions in real and lattice units respectively. The wetting on the solid boundaries at the base of the pillars is achieved using the surface energy density ψ_s, where

$$\psi_s = \sum_{i=1}^{3} 12\gamma_{is}\left(\frac{1}{2}C_i^2 - \frac{2}{3}C_i^3 + \frac{1}{4}C_i^4\right), \tag{21}$$

where γ_{is} is the interfacial tension of component i on the solid surface.

To minimise the free energy numerically, Ψ in Eq. (15) is discretised, as shown previously[57], into a cubic array of lattice points, with the grid spacing equal to the interface width ϵ. To create the smooth, solid array of pillars in the diffuse interface method, we firstly initialise component 1 in the desired pattern of cylinders. The rest of the system is filled with pure gas (C_3), and the liquid component (C_2) is fixed at 0. ψ_g and ψ_s are also set to zero. The energy minimisation is then carried out on this initial system using the memory- and computationally efficient L-BFGS algorithm[58,59]. We truncate the algorithm to 30 iterations, as this allows the 1–3 diffuse interface to form, without allowing the relaxing component 1 to alter the desired shape of the cylinder.

Next, the solid surfaces at the base of the pillars are introduced, and the gravitational energy density switched on. Component 2 (the liquid phase) is initialised in the system in a prescribed configuration. The solid phase (C_1) is now fixed while the liquid (C_2) and gas phases (C_3) are allowed to vary. Ψ in Eq. (15) is now minimised under these constraints. The minimisation is deemed to have converged based on an rms gradient condition: when $|\nabla \Psi| < 10^{-5}$.

For the square pillars, the solid boundaries of the posts conform to the discretisation lattice. This means that we do not need to apply the diffuse solid method, and instead treat all solid boundaries using Eq. (19). C_1 is fixed at 0 throughout the minimisation, so the ternary model in Eq. (15) reduces to a binary liquid-gas model.

Data availability

Code availability

The phase field model software is available from the corresponding author upon reasonable request.

References

1. Comanns, P. Passive water collection with the integument: mechanisms and their biomimetic potential. *J. Exp. Biol.* **221**, jeb153130 (2018).
2. Sherbrooke, W. C. Rain-Drinking Behaviors of the Australian Thorny Devil (Sauria: Agamidae). *J. Herpetol.* **27**, 270 (1993).
3. Comanns, P., Withers, P. C., Esser, F. J. & Baumgartner, W. Cutaneous water collection by a moisture-harvesting lizard, the thorny devil (Moloch horridus). *J. Exp. Biol.* **219**, 3473–3479 (2016).
4. Comanns, P. et al. Adsorption and movement of water by skin of the Australian thorny devil (Agamidae: Moloch horridus). *R. Soc. Open Sci.* **4**, 170591 (2017).
5. Horiguchi, H., Hironaka, M., Meyer-Rochow, V. B. & Hariyama, T. Water Uptake via Two Pairs of Specialized Legs in Ligia exotica (Crustacea, Isopoda). *Biol. Bull.* **213**, 196–203 (2007).
6. Chen, H. et al. Continuous directional water transport on the peristome surface of Nepenthes alata. *Nature* **532**, 85–89 (2016).
7. Şahmaran, M. & Li, V. C. Influence of microcracking on water absorption and sorptivity of ECC. *Mater. Struct.* **42**, 593–603 (2009).
8. Tang, S., Yao, Y., Andrade, C. & Li, Z. Recent durability studies on concrete structure. *Cem. Concr. Res.* **78**, 143–154 (2015).
9. Bao, J. & Wang, L. Capillary imbibition of water in discrete planar cracks. *Constr. Build. Mater.* **146**, 381–392 (2017).
10. Zhang, P., Wittmann, F. H., Vogel, M., Müller, H. S. & Zhao, T. Influence of freeze-thaw cycles on capillary absorption and chloride penetration into concrete. *Cem. Concr. Res.* **100**, 60–67 (2017).
11. Sidiq, A., Gravina, R. & Giustozzi, F. Is concrete healing really efficient? A review. *Constr. Build. Mater.* **205**, 257–273 (2019).
12. van Breugel, K. Is there a market for self-healing cement-based materials? In *Proc. First Int. Conf. Self Heal. Mater.* (eds. Schmets, A. J. M. & Zwaag, V. D. S.) 1–9 (Science+Business Media, Springer, 2007).
13. American Society of Civil Engineers. 2017 Infrastructure Report Card: A comprehensive assessment of America's Infrastructure. Tech. Rep. (2017). https://www.infrastructurereportcard.org/.
14. Medved', I. & Černý, R. Modeling of radionuclide transport in porous media: a review of recent studies. *J. Nucl. Mater.* **526**, 151765 (2019).
15. Suzuki, A., Fomin, S., Chugunov, V. & Hashida, T. Mathematical Modeling of Non-Fickian Diffusional Mass Exchange of Radioactive Contaminants in Geological Disposal Formations. *Water* **10**, 123 (2018).
16. Hodgkinson, D. et al. An overview of Task 6 of the Äspö Task Force: modelling groundwater and solute transport: improved understanding of radionuclide transport in fractured rock. *Hydrogeol. J.* **17**, 1035–1049 (2009).
17. Young, T. An Essay on the Cohesion of Fluids. *Philos. Trans. R. Soc. London* **95**, 65–87 (1805).
18. marquis de Laplace, P. S. *Traité de Mécanique Céleste*, Volume 4. chap. Supplément au dixième livre du Traité de Mécanique Céleste (Courcier, Paris, France, 1805).
19. Gibbs, J. W. *The Scientific Papers of J. Willard Gibbs*, Volume 1. Thermodynamics (Longmans, Green and Co., 1906).
20. de Gennes, P. G. Wetting: Statistics and Dynamics. *Rev. Mod. Phys.* **57**, 827–863 (1985).
21. de Gennes, P.-G., Brochard-Wyart, F. & Quéré, D. *Capillarity and Wetting Phenomena.* (Springer New York, New York, NY, 2004).
22. Bico, J., Tordeux, C. & Quéré, D. Rough wetting. *Europhys. Lett.* **55**, 214–220 (2001).
23. Bico, J., Thiele, U. & Quéré, D. Wetting of textured surfaces. *Coll. Surf. A: Physicochem. Eng. Aspects* **206**, 41–46 (2002).
24. Quéré, D. Rough ideas on wetting. *Phys. A Stat. Mech. Appl.* **313**, 32–46 (2002).
25. Quéré, D. Wetting and Roughness. *Annu. Rev. Mater. Res.* **38**, 71–99 (2008).
26. Bico, J. & Quéré, D. Precursors of impregnation. *Europhys. Lett.* **61**, 348–353 (2003).
27. Kim, J., Moon, M. W. & Kim, H. Y. Dynamics of hemiwicking. *J. Fluid Mech.* **800**, 57–71 (2016).
28. Brabazon, J. et al. Rock Fracture Sorptivity as Related to Aperture Width and Surface Roughness. *Vadose Zone J.* **18**, 1–10 (2019).
29. Li, C. et al. Bioinspired inner microstructured tube controlled capillary rise. *Proc. Natl. Acad. Sci.* **116**, 12704–12709 (2019).
30. Pezron, I., Bourgain, G. & Quéré, D. Imbibition of a Fabric. *J. Coll. Interfac. Sci.* **173**, 319–327 (1995).
31. Parada, M., Zhou, X., Derome, D., Rossi, R. M. & Carmeliet, J. Modeling wicking in textiles using the dual porosity approach. *Text. Res. J.* **89**, 3519–3528 (2019).
32. Kim, J., Moon, M. W. & Kim, H. Y. Capillary rise in superhydrophilic rough channels. *Phys. Fluids* **32**, 032105 (2020).
33. Cassie, A. B. D. & Baxter, S. Wettability of Porous Surfaces. *Trans. Faraday. Soc.* **40**, 546–551 (1944).
34. Wenzel, R. N. Resistance of solid surfaces to wetting by water. *Ind. Eng. Chem.* **28**, 988–994 (1936).
35. Gardner, D., Jefferson, A. & Hoffman, A. Investigation of capillary flow in discrete cracks in cementitious materials. *Cem. Concr. Res.* **42**, 972–981 (2012).
36. Shen, A., Liu, Y., Qiu, X., Lu, Y. & Liang, S. A model for capillary rise in nano-channels with inherent surface roughness. *Appl. Phys. Lett.* **110**, 121601 (2017).
37. Wang, L., Li, N., Tian, Y., Liu, N. & Xu, S. Experimental study of capillary water migration in vertically parallel-plate fractures in rock masses in cold regions. *Arab. J. Geosci.* **15**, 128 (2022).
38. Chen, H. et al. Ultrafast water harvesting and transport in hierarchical microchannels. *Nat. Mater.* **17**, 935–942 (2018).
39. Ahn, J.-H. et al. 3D-printed biodegradable composite scaffolds with significantly enhanced mechanical properties via the combination of binder jetting and capillary rise infiltration process. *Addit. Manuf.* **41**, 101988 (2021).
40. Dudukovic, N. A. et al. Cellular fluidics. *Nature* **595**, 58–65 (2021).
41. Zhang, W., Zheng, Q., Ashour, A. & Han, B. Self-healing cement concrete composites for resilient infrastructures: a review. *Compos. Part B Eng.* **189**, 107892 (2020).
42. Yeganeh, M. S. et al. Solid with infused reactive liquid (SWIRL): a novel liquid-based separation approach for effective CO$_2$ capture. *Sci. Adv.* **8**, eabm0144 (2022).
43. Raeesi, B., Morrow, N. R. & Mason, G. Effect of surface roughness on wettability and displacement curvature in tubes of uniform cross-section. *Coll. Surf. A: Physicochem. Eng. Aspects* **436**, 392–401 (2013).

44. Tang, L.-H. & Tang, Y. Capillary rise in tubes with sharp grooves. *J. Phys. II* **4**, 881–890 (1994).
45. Forsberg, P. S. H., Priest, C., Brinkmann, M., Sedev, R. & Ralston, J. Contact Line Pinning on Microstructured Surfaces for Liquids in the Wenzel State. *Langmuir* **26**, 860–865 (2010).
46. Liu, S., Li, S. & Liu, J. Jurin's law revisited: Exact meniscus shape and column height. *Eur. Phys. J. E* **41**, 46 (2018).
47. de Wijs, W.-J. A., Laven, J. & de With, G. Wetting forces and meniscus pinning at geometrical edges. *AIChE J.* **62**, 4453–4465 (2016).
48. Seemann, R., Brinkmann, M., Kramer, E. J., Lange, F. F. & Lipowsky, R. Wetting morphologies at microstructured surfaces. *Proc. Natl. Acad. Sci.* **102**, 1848–1852 (2005).
49. Wu, L. et al. Highly efficient three-dimensional solar evaporator for high salinity desalination by localized crystallization. *Nat. Commun.* **11**, 521 (2020).
50. Singh, S. C. et al. Solar-trackable super-wicking black metal panel for photothermal water sanitation. *Nat. Sustain.* **3**, 938–946 (2020).
51. Lowengrub, J. & Truskinovsky, L. Quasi-incompressible Cahn-Hilliard fluids and topological transitions. *Proc. R. Soc. London. Ser. A Math. Phys. Eng. Sci.* **454**, 2617–2654 (1998).
52. Panter, J. R. & Kusumaatmaja, H. The impact of surface geometry, cavitation, and condensation on wetting transitions: posts and reentrant structures. *J. Phys. Condens. Matter* **29**, 084001 (2017).
53. Panter, J. R., Gizaw, Y. & Kusumaatmaja, H. Multifaceted design optimization for superomniphobic surfaces. *Sci. Adv.* **5**, eaav7328 (2019).
54. Boyer, F. & Lapuerta, C. Study of a three component Cahn-Hilliard flow model. *ESAIM Math. Model. Numer. Anal.* **40**, 653–687 (2006).
55. Semprebon, C., Krüger, T. & Kusumaatmaja, H. Ternary free-energy lattice Boltzmann model with tunable surface tensions and contact angles. *Phys. Rev. E* **93**, 033305 (2016).
56. Shimizu, R. & Tanaka, H. Impact of complex topology of porous media on phase separation of binary mixtures. *Sci. Adv.* **3**, eaap9570 (2017).
57. Kusumaatmaja, H. Surveying the free energy landscapes of continuum models: application to soft matter systems. *J. Chem. Phys.* **142**, 124112 (2015).
58. Nocedal, J. Updating quasi-Newton matrices with limited storage. *Math. Comp.* **35**, 773–782 (1980).
59. Liu, D. & Nocedal, J. On the limited memory BFGS method for large scale optimization. *Math. Program.* **45**, 503–528 (1989).
60. Kusumaatmaja, H. Rough capillary rise [dataset] (2023). Durham University, https://doi.org/10.15128/r20p096694s.

Acknowledgements

Author contributions
J.R.P. and M.S.Y. developed the Dual-Rise model, with contributions from A.R.K., A.J., and H.K. J.R.P. designed and performed the simulations and analysed the simulation data. A.R.K. and M.A.K. designed and performed the experiments and analysed the experimental data. J.R.P. collated and presented the data, and wrote the paper with A.R.K. All authors contributed to editing the paper. H.K., A.J., and M.S.Y. conceptualised the project. H.K. and A.J. were responsible for project management.

Competing interests
The authors declare no competing interests.

Additional information
Supplementary information The online version contains supplementary material available at https://doi.org/10.1038/s42005-023-01160-w.

Correspondence and requests for materials should be addressed to Halim Kusumaatmaja.

Peer review information *Communications Physics* thanks the anonymous reviewers for their contribution to the peer review of this work. Peer reviewer reports are available.

Reprints and permission information is available at http://www.nature.com/reprints

Publisher's note Springer Nature remains neutral with regard to jurisdictional claims in published maps and institutional affiliations.